

Model Hamiltonian parameters for half-metallic ferromagnets NiMnSb and CrO₂A. Yamasaki,¹ L. Chioncel,^{2,3} A. I. Lichtenstein,⁴ and O. K. Andersen¹¹Max-Planck-Institut für Festkörperforschung Heisenbergstrasse 1, D-70569 Stuttgart, Germany²Department of Physics, University of Orléans, 410087 Orléans, France³Institute for Theoretical Physics and Computational Physics,
Graz University of Technology, A-8010 Graz, Austria⁴Institute of Theoretical Physics, University of Hamburg, Germany

(Dated: Received 10 March 2006; revised manuscript received 25 May 2006)

Using the recently developed Nth-order multi-orbital (NMO) based downfolding technique we revisit the electronic properties of half-metallic ferromagnets, the semi-Hausler NiMnSb and rutile CrO₂. The NMO Wannier orbitals for the Mn-d and Cr-t_{2g} manifolds are constructed and the mechanism of chemical bonding is discussed. The effective hopping Hamiltonian parameters are calculated using a NMO downfolded basis set. We propose model Hamiltonian parameters with possibly minimal basis sets for both half-metallic ferromagnetic alloys.

PACS numbers: 75.50.Cc, 71.10.-w, 71.20.Lp, 71.15.Ap

I. INTRODUCTION

Half-metallic ferromagnets (HMF) such as the semi-Hausler NiMnSb or the rutile CrO₂ are a subject of strongly growing interest mainly due to their potential applications in spin-dependent electronics, so-called "spintronics".^{1,2,3,4} Concerning their electronic structure, half-metallic materials exhibit a gap in one spin channel and a normal metallic behavior for the opposite spin bands. This means that electrons at the Fermi level are 100% spin polarized. Much experimental effort is devoted to the semi-Hausler NiMnSb compound, although highly spin-polarized carrier injection has not yet been achieved. At low temperatures superconducting point contact measurements revealed a less than 50% polarization of valence electrons.^{5,6} Similar values were obtained by spin resolved photoemission,⁷ and more recently experiments using the synchrotron radiation showed at room temperature a 40% polarization at the Fermi level.⁸ This discrepancy in comparison with the predicted half-metallic behavior is attributed to interface and surface effects. However, by a proper engineering, half-metallicity can be restored at surface/interfaces.⁹ The experimental evidence for half-metallicity is stronger in CrO₂: Andreev reflection,¹⁰ superconducting tunneling,¹¹ photoemission,¹² and point-contact magnetoresistance,¹³ all give values of polarization in the range 85–100%. Keizer et al. have injected new excitement into the field of half-metals, by reporting the existence of a spin triplet supercurrent through the strong ferromagnet CrO₂.¹⁴

Future spin electronic devices based on HMF will probably be expected to work around and above room temperature, so one of the essential requirements is that these ferromagnets should have quite high Curie temperatures. Both NiMnSb (T_c = 730 K) and CrO₂ (T_c = 400 K) fulfill this requirement. A second essential requirement for using half-metallic materials in practical devices could be the understanding of finite-temperature behavior of spin polarization both from the experimental and the theoret-

ical point of view.

On the theoretical side, HMF have been strongly supported by first-principles calculations, based on density-functional theory.⁴ These calculations offer a proper description of the ground state properties, and are usually performed for zero temperatures. One way to approach the finite temperature behavior is based on modeling the many-body interactions in the real material, therefore the evaluation of the model Hamiltonian parameters is required. These parameters constitute the starting point for a finite-temperature full many-body microscopic description. The local density approximation (LDA) electronic structure allows us to evaluate the effective hopping parameters, to which a Hubbard type interaction is added to construct the starting Hamiltonian. In the multi-orbital case the Hubbard Hamiltonian is described by

$$\hat{H}^{\text{int}} = \frac{1}{2} \sum_{i,m} U_{i,m} \hat{n}_{i,m} \hat{n}_{i,m} + \frac{1}{2} \sum_{i,m} (U_{i,m} - J_{i,m}) \hat{n}_{i,m} \hat{n}_{i,m}; \quad (1)$$

where i is the spin index, m are local orbitals at site i . The on-site Coulomb interactions are expressed in terms of two parameters: $U_{i,m} = U$, $U_{i,m}(m) = U - 2J$, and $J_{i,m} = J$.¹⁵ This model Hamiltonian is defined on a basis set of local orbitals and thus the microscopic interactions are local, involving a small number of electrons and a small number of orbitals. A numerically exact solution of this model is achieved by the quantum Monte Carlo solver in the framework of the dynamical mean field theory (DMFT).^{16,17} We used the recently developed LDA+DMFT methods^{15,18,19,20,21,22} in order to investigate finite-temperature many-body effects for the practically important spintronic materials such as the semi-Hauslers NiMnSb,²³ FeMnSb,²⁴ and the zinc-blende CrAs (Ref. 25) and VAs.²⁶ In these materials, due to their half-metallic ferromagnetic band structure, the incoherent [nonquasiparticle (NQP)] states play an important

role. The NQP states were considered theoretically for the first time by Edwards and Hertz²⁷ in the framework of broad-band Hubbard model for itinerant electron ferromagnets.

For the realistic electronic structure of NM nSb NQP states are situated just above the Fermi level for the minority spin channel, having a considerable spectral weight.²³ In FeM nSb the spectral weight of NQP states is enhanced in comparison with NM nSb, producing a drastic depolarization at the Fermi level.²⁴ For CrAs in the zinc-blende structure,²⁵ the spectral weight of NQP states was studied in connection with the substrate lattice parameter. For large substrate lattice parameters the Fermi level is situated close to the middle of the minority spin gap and the NQP states are clearly visible. However, for smaller substrate lattice parameters the NQP contribution is negligible. VAs in a similar zinc-blende structure is predicted by LDA/GGA to be a narrow gap semiconductor.²⁹ In addition to the presence of NQP states, many-body interactions determine the closure of the semiconducting majority spin gap, leading to a half-metallic ferromagnetic ground state.²⁶ Therefore, a correct prediction of new spintronic materials should take into account finite-temperature many-body correlation effects, which might play an essential role in depolarization.

In order to further investigate the nature of the NQP state, a realistic model Hamiltonian is required. In this paper we will use the recently developed massive downfolding scheme^{30,31} in order to produce real space Hamiltonian parameters for both NM nSb and CrO₂ half-metallic compounds.

The paper is organized as follows. Section II describes briefly the computational details of the Nth-order multiorbital (NMTO) method. The corresponding subsections IIA and IIB present the results of downfolding onto the Mn-d, Cr-t_{2g} manifolds, respectively, and gives the values of the effective hopping parameters. In the case of CrO₂ we compare the results of the matrix elements of the effective hopping Hamiltonian in two distinct Wannier orbitals basis sets: the one which describes the full Cr-t_{2g} manifold and a second in which d_{xy} and d_{yz} orbitals could be described individually. The values of the effective Coulomb interaction parameters are given in Sec. III. In the summary we discuss the construction of possible model Hamiltonians with a minimal basis set for both half-metallic ferromagnets.

II. EFFECTIVE HOPPING PARAMETERS

In the present paper we use the NMTO method^{30,31} for generation of localized Wannier functions. The NMTO method can be used to generate truly minimal basis sets with massive downfolding technique. Downfolding produces minimal bands which follow exactly the bands obtained with the large basis set. In the case of NM nSb and CrO₂, Mn-d and Cr-t_{2g} form the minimal basis set.

TABLE I: The multiorbital radii for NM nSb and CrO₂. The radii of the empty spheres E are also given. The second row corresponds to the LMTO basis sets used in the self-consistent calculation of LDA potential. (l) means that the l-partial waves were downfolded within the LMTO-ASA + cc.

	NM nSb			
	Ni	Mn	Sb	E
R _{MT} (a.u.)	2.584	2.840	2.981	2.583
basis set	spd	spd	sp(df)	sp(d)
	CrO ₂			
	Cr	O	E	El
R _{MT} (a.u.)	2.213	2.094	1.653	1.566
basis set	spd	(s)p(d)	s(p)	s(p)

The truly minimal set of symmetrically orthonormalized NMTOs is a set of Wannier functions. In the construction of the NMTO basis set the active channels are forced to be localized onto the eigenchannel R_m, therefore the NMTO basis set is strongly localized.

Fourier transformation of the orthonormalized NMTO Hamiltonian, $H^{\text{LDA}}(\mathbf{k})$, yields on-site energies and hopping integrals,

$$H_{0m0,Rm}^{\text{LDA}} = \int_{0m0} H^{\text{LDA}} \psi_{Rm}^* \psi_{0m0} = t_{m0,Rm}^{xyz}; \quad (2)$$

in a Wannier representation, where the NMTO Wannier function ψ_{Rm} is orthonormal.

The matrix element between orbitals m^0 and m , both on site $R^0 = R = 0$, is $t_{m0,m}^0$, and the hopping integral from orbital m^0 on site $R^0 = 0$ to orbital m on site $R = (x;y;z)$ is $t_{m0,Rm}^{xyz}$.

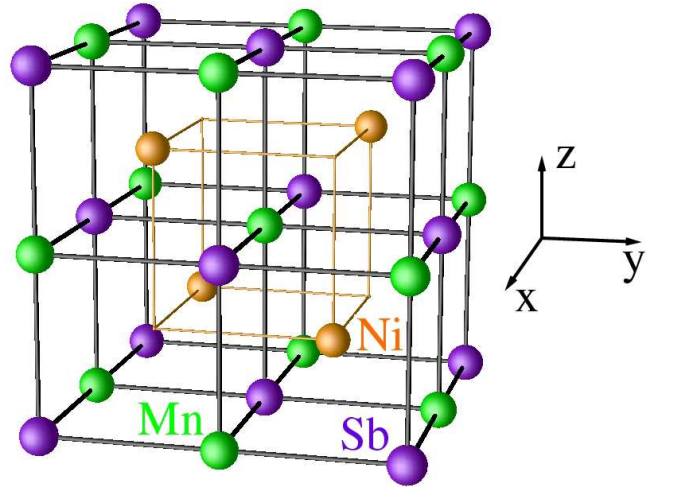


FIG. 1: (Color online) CrO₂ structure with the fcc Bravais lattice (space group Fm-3m). Mn (green) and Sb (purple) atoms are located at (0, 0, 0) and ($\frac{1}{2}, \frac{1}{2}, \frac{1}{2}$) forming the rocksalt structure arrangement. Ni (orange) atom is located in the octahedrally coordinated pocket, at one of the cube center positions ($\frac{3}{4}, \frac{3}{4}, \frac{3}{4}$) leaving the other ($\frac{1}{4}, \frac{1}{4}, \frac{1}{4}$) empty. This creates voids in the structure.

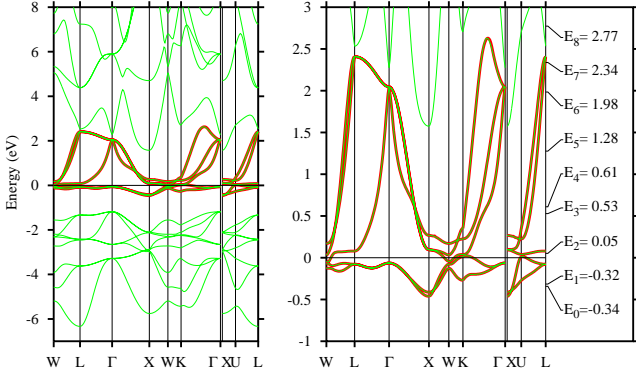


FIG. 2: (Color online) The band structure of non-spin-polarized NiMnSb calculated with the full basis is given in thick (green) line. The thin (red) band have been calculated with a M n-d NMTO basis set. Fermi energy E_F is set to be zero. The high-symmetry points are W ($\frac{1}{2}; 1; 0$), L ($\frac{1}{2}; \frac{1}{2}; \frac{1}{2}$), (0;0;0), X (0;1;0), K ($\frac{3}{4}; \frac{3}{4}; 0$), in the W-L-X-W-K line and X (0;0;1), U ($\frac{1}{4}; \frac{1}{4}; 1$), L ($\frac{1}{2}; \frac{1}{2}; \frac{1}{2}$), in the X-U-L line. Energy mesh used for downfolded calculation is given in the right of the band structure with a unit of eV.

The LDA potential is generated with the Stuttgart TB-LMTO-ASA code (the LMTO-ASA including the combined correction).^{32,33,34} NMTO calculations are performed using the generated LDA potentials. The radii of MT potential spheres and the LMTO bases used in the calculation for NiMnSb and CrO₂ are listed in Table I. For the detail of the calculation, see the appendixes of Ref. [35].

A. Downfolding onto the M n-d manifold in NiMnSb

The intermetallic compound NiMnSb crystallizes in the cubic structure of MgAg₃ type (C_{1b}) with the fcc Bravais lattice (space group $F\bar{4}3m = T_d^2$). The crystal structure is shown in Fig. 1. This structure can be described as three interpenetrating fcc lattices of Ni, Mn, and Sb. The Ni and Sb sublattices are shifted relative to the Mn sublattice by a quarter of the [111] diagonal in opposite directions. In the present calculation the experimental lattice constant of NiMnSb ($a = 5.927$ Å) is used.

A detailed description of the band structure of semi-Heusler alloys was given using electronic structure calculations and tight-binding model analysis,^{4,36,37,38,39} and we briefly summarize the results. The key points, which determine the behavior of electrons near the Fermi level for the half-metallic property, are the interplay between the crystal structure, valence electron count, covalent bonding and large exchange splitting of the M n-d electrons.

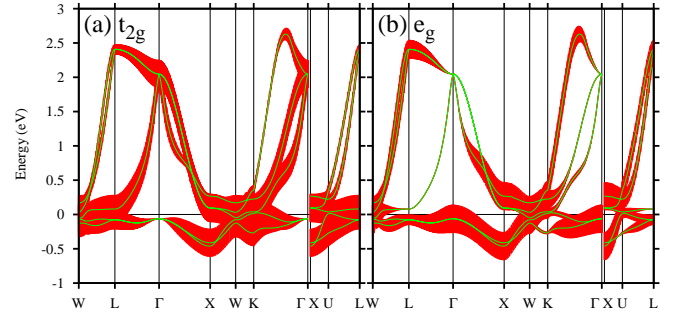


FIG. 3: (Color online) The NMTO band structure calculated with a M n-d NMTO basis set. The bands have been decorated with (a) t_{2g} and (b) e_g characters. About symmetry points and E_F , see Fig. 2.

1. Chemical bonding and the M n-d Wannier orbitals

In the nonmagnetic phase the C_{1b} compounds have a d-d gap resulting from covalent hybridization of the higher-valent transition metal (Ni) with the lower-valent transition metal (Mn). For the minority spin gap opening, not only the M n-d-Sb-p interactions, but also M n-d-Ni-d interactions have to be taken into account. Moreover the loss of inversion symmetry produced by C_{1b} structure (the symmetry lowering from O_h in the L₂₁ structure to T_d in the C_{1b} structure at Mn site) is an essential additional ingredient. All the above interactions combined with the T_d symmetry lead to a nonzero anti-crossing of bands and to the gap opening. The existence of sp-valent Sb is crucial to provide stability to this compound.

Based on the understanding of the bonding in the NiMnSb, we propose a downfolding scheme in which all orbitals of all atoms except M n-d is downfolded.

In Fig. 2 the non-spin-polarized band structure of NiMnSb is calculated with the full basis set (thick green line). M n-d, Ni-d, and Sb-p states are lying between 0.5{2.5 eV, 3{1 eV, and 6.5{3 eV, respectively. Sb-s states are sitting around 12{10 eV, that is not shown in Fig. 2. There is an excellent agreement with the previous calculations.⁴ The thin red band has been calculated with the downfolded basis set which includes only M n-d orbitals. The energy mesh used in the downfolded calculation is given to the right of the band structure. The two sets of bands are identical. In Fig. 3 the band structures of NiMnSb with the orbital character projected on to NMTO t_{2g} and e_g Wannier orbitals are shown. The fatness associated with each band is proportional to the character of the orbital. The strong hybridization between t_{2g} and e_g states is clearly seen. NMTO M n-d Wannier orbitals are shown in Fig. 4. The triply degenerate manganese t_{2g} orbitals are very complicated due to the hybridization with Ni-d and Sb-p states. The d_{xy} orbital at Mn site is deformed by antibonding with the Ni-d state directed tetrahedrally to [111], $\bar{1}\bar{1}\bar{1}$, [111], and $\bar{1}\bar{1}\bar{1}$. The same Ni-d orbitals couple with Sb-

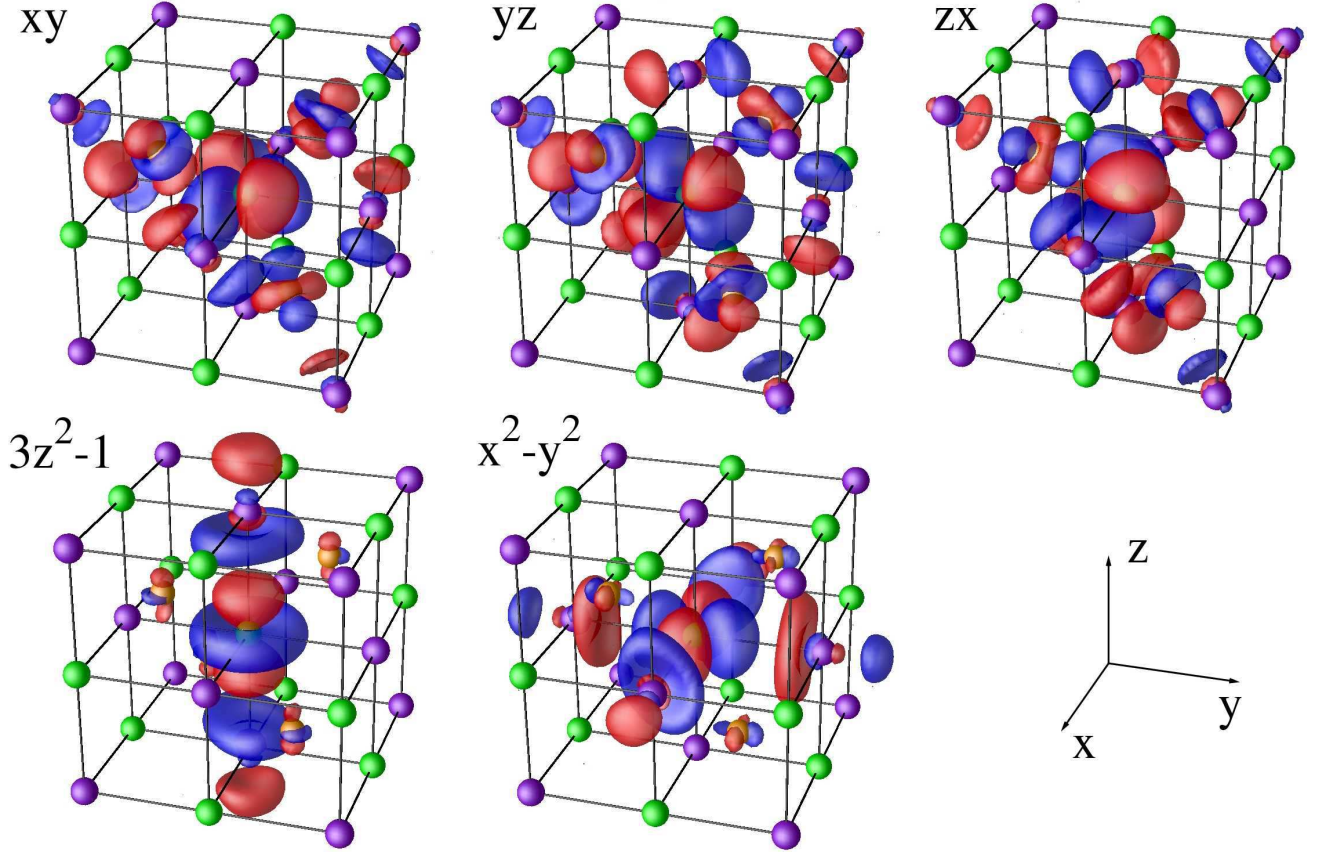


FIG. 4: (Color) NM TO M n-d Wannier orbitals of NM nSb. Ni is orange, Mn is green, and Sb is purple. Red (blue) indicates a positive (negative) sign. Upper panel: t_{2g} orbitals; d_{xy} (left), d_{yz} (middle), d_{zx} (right). The triply degenerate t_{2g} orbitals can be obtained by the permutation of axes. Lower panel: e_g orbitals; d_{3z^2-1} (left), $d_{x^2-y^2}$ (middle). These e_g orbitals are doubly degenerated.

p states. The direct Mn- d_{xy} -Sb-p coupling is not seen since the distance is $d(\text{Mn-Sb})$ and $d(\text{Ni-Sb}) = 1\sqrt{\frac{3}{2}}$. Therefore the Ni-d-Sb-p interactions are more favorable. The dispersion of the Mn t_{2g} bands is mainly due to hopping via the tails of Sb-p and Ni-d orbitals. On the other hand, the second nearest neighbor (NN) d-d hopping of t_{2g} orbital is small. The e_g orbitals at Mn site are much easier to understand: they point towards Sb atoms, and a strong pd coupling between Sb-p and Mn- e_g states is seen. This induces large second NN d-d hoppings.

2. Effective hopping matrix elements in the basis set of Mn-d Wannier orbitals

In the many-body picture the Mn t_{2g} and e_g constitutes the active orbitals which are responsible for the low-energy physics, having fluctuation in occupation and spins. The effective hopping Hamiltonian matrix elements built up with these active orbitals are as follows.

NM TO basis set:

$$|i\rangle = |xyi; yzi; xzi; 3z^2-1i; x^2-y^2i\rangle \quad (3)$$

The on-site term :

$$t_{m_0 m_0}^{000} = \begin{pmatrix} 0 & 360 & 0 & 0 & 0 & 0 \\ 360 & 0 & 0 & 0 & 0 & 0 \\ 0 & 0 & 360 & 0 & 0 & 0 \\ 0 & 0 & 0 & 434 & 0 & 0 \\ 0 & 0 & 0 & 0 & 434 & 0 \end{pmatrix} : \quad (4)$$

The first nearest neighbor:

$$t_{m_0 m_0}^{0\frac{1}{2}\frac{1}{2}} = \begin{pmatrix} 0 & 129 & 2 & 23 & 100 & 12 \\ 129 & 2 & 51 & 2 & 75 & 130 \\ 2 & 51 & 2 & 129 & 40 & 92 \\ 23 & 2 & 129 & 40 & 92 & 37 \\ 100 & 75 & 40 & 9 & 37 & 0 \\ 12 & 130 & 92 & 37 & 0 & 51 \end{pmatrix} : \quad (5)$$

The second nearest neighbor:

$$t_{m_0 m_0}^{001} = \begin{pmatrix} 0 & 16 & 0 & 0 & 43 & 0 \\ 16 & 0 & 4 & 0 & 0 & 0 \\ 0 & 4 & 0 & 4 & 0 & 0 \\ 0 & 0 & 4 & 0 & 0 & 0 \\ 43 & 0 & 0 & 229 & 0 & 0 \\ 0 & 0 & 0 & 0 & 0 & 4 \end{pmatrix} ; \quad (6)$$

where the unit is meV, $E_F = 0$, and hopping integrals up to the second NN are shown. The on-site term $t_{m_0 m_0}^{000}$ is

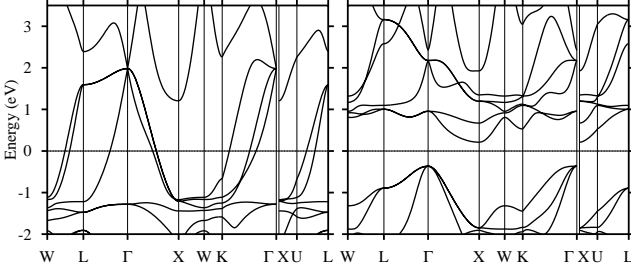


FIG. 5: Full basis set spin-polarized (ferromagnetic) bands for NM nSb; majority spin (left) and minority spin (right). About symmetry points and E_F , see Fig. 2. The similarity of the spin-polarized majority with the non-spin-polarized bands is evidenced.

diagonal, t_{2g} and e_g orbitals are triply and doubly degenerated, respectively. The crystal-field splitting between t_{2g} and e_g orbitals is 74 meV. There are 12 first NN and 6 second NN hoppings. Only one hopping integral at each NN is shown, but all the hopping integrals can be derived from proper unitary transformation due to the crystal symmetry. For details, see Ref. [35]. The hopping between t_{2g} and e_g orbitals is strongly influenced by the presence of tails belonging to the Sb-p and Ni-d orbitals. Due to these tails large values of t_{2g} to e_g hoppings are evidenced in Eqs. (5) and (6). We mention that these hoppings should be small for the case of "pure" t_{2g} and e_g orbitals. In addition, due to the presence of Sb-p and Ni-d tails t_{2g} and e_g orbitals are not divided clearly as seen in Fig. 3. Therefore they should be treated equally. Hoppings further than third NN are small; for instance, the largest values are 66 (third) and 56 meV (fourth), a small number of matrix elements of the hoppings are less than 30 meV, and the others are almost zero in the third and fourth NN hoppings. Further NN hoppings are negligible.

In this procedure, we obtained the nonzero hopping matrix elements between the all Mn-d orbitals, in the downfolded representation. The numbers of independent parameters of the effective model are equal to the number of matrix elements from Eqs. (4)–(6).

We now consider the spin-polarized case. Systems with 18 valence electrons per unit cell are semiconductors, but when they contain more than 18 electrons (22 electrons in NM nSb, that is, Ni $3d^8 4s^2$, Mn $3d^5 4s^2$, and Sb $5s^2 5p^3$), antibonding states are populated. Therefore, the non-magnetic phase becomes unstable and the magnetic state can be stabilized. The large exchange splitting of the Mn atom (producing a magnetic moment of around 3.7 μ_B) is crucial to induce a half-metallic property. As we saw before, for the nonmagnetic case, the t_{2g} and e_g states of Ni are situated around 2 eV below E_F . In the spin-polarized calculation their position is slightly changed, therefore the exchange splitting on Ni is not large. The actual magnetic moment calculation gives a value around 0.3 μ_B .

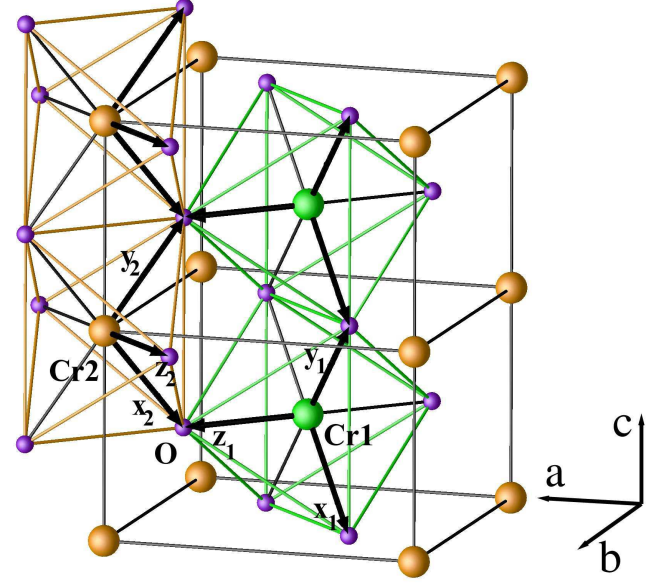


FIG. 6: (Color online) CrO_2 (rutile) structure. Cr1 (green) and Cr2 (orange) are located at $(0, 0, 0)$ and $(\frac{1}{2}; \frac{1}{2}; \frac{1}{2})$. Cr atoms are octahedrally coordinated by oxygen atoms (purple). The local coordinate system is used for each Cr atom; $\hat{x}_1 = \frac{1}{2}\hat{a} + \frac{1}{2}\hat{b} - \frac{1}{2}\hat{c}$, $\hat{y}_1 = \frac{1}{2}\hat{a} + \frac{1}{2}\hat{b} + \frac{1}{2}\hat{c}$, $\hat{z}_1 = \frac{1}{2}\hat{a} + \frac{1}{2}\hat{b}$, and $\hat{x}_2 = \frac{1}{2}\hat{a} - \frac{1}{2}\hat{b} - \frac{1}{2}\hat{c}$, $\hat{y}_2 = \frac{1}{2}\hat{a} - \frac{1}{2}\hat{b} + \frac{1}{2}\hat{c}$, $\hat{z}_2 = \frac{1}{2}\hat{a} + \frac{1}{2}\hat{b}$. $\hat{x}_{1,2}$ and $\hat{y}_{1,2}$ are approximately point to O atom, and $\hat{z}_{1,2}$ are exactly point to O atom. The local axis is transformed into each other by a rotation of 90° around the crystal c axis.

The non-spin-polarized result has a striking resemblance to the majority spin-polarized calculations, presented in Fig. 5. Kulatov et al. explained half-metallicity of NM nSb and CrO_2 by the extended Stoner factor calculations in the rigid-band approximation;³⁹ their minority spin-band gap opens due to the exchange splitting, which shifts minority bands, so they become empty. According to our results, the NM TO antibonding orbitals should be a good description for the empty Mn-d states in the minority channel.

All the above results suggest that a minimal basis set which captures the essential physics in NM nSb can be constructed using Mn t_{2g} and e_g states. Therefore, the non-spin-polarized result with Mn-d orbitals can be a good starting point for the many-body calculations.

B. Downfolding onto the Cr-d manifolds in CrO_2

Chromium dioxide CrO_2 has a rutile (tetragonal) structure with $a = 4.421 \text{ \AA}$, $c = 2.916 \text{ \AA}$ ($c/a = 0.65958$), and internal parameter $u = 0.3053$.⁴⁰ The Cr atoms form a body-center tetragonal lattice and are surrounded by a slightly distorted octahedron of oxygen atoms. The space group of this compound is nonsymmorphic ($P4_2/mnm = D_{4h}^{14}$). Cr^{4+} has a close shell Ar core and two additional

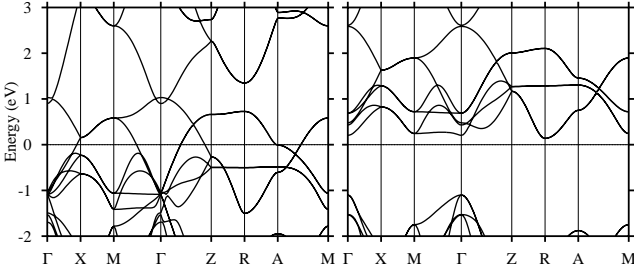


FIG. 7: Full basis set spin-polarized (ferromagnetic) bands for CrO_2 ; majority spin (left) and minority spin (right). E_F is set to be zero. The high-symmetry points are Γ (0;0;0), X $(0;\frac{1}{2};0)$, M $(\frac{1}{2};\frac{1}{2};0)$, Z $(0;0;\frac{1}{2})$, R $(0;\frac{1}{2};\frac{1}{2})$, A $(\frac{1}{2};\frac{1}{2};\frac{1}{2})$.

3d electrons. The Cr ions are in the center of the CrO_6 octahedra so the 3d orbitals are split into a t_{2g} triplet and an excited e_g doublet. With only two 3d electrons the e_g states are irrelevant and only the t_{2g} orbitals need to be considered. The tetragonal symmetry distorts the octahedra, which lifts the degeneracy of the t_{2g} orbitals into a d_{xy} ground state and $d_{yz}+d_{zx}$ and $d_{yz}-d_{zx}$ excited states,^{41,42} where a local coordinate system is used for every octahedron (see Fig. 6). A double exchange mechanism for the two electrons per Cr site was proposed⁴³ in which due to the strong Hund's rule corroborated with the distortion of CrO_6 octahedra leads to the localization of the one electron into the d_{xy} orbital, while the electrons in the d_{yz} and d_{xz} are itinerant.

Measurements of the magnetic susceptibility in the paramagnetic phase show a Curie-Weiss-like behavior indicating the presence of local moments,⁴⁴ suggesting a mechanism of ferromagnetism beyond the standard band or Stoner-like model.

Several recent experiments including photoemission,⁴⁵ soft x-ray absorption,⁴⁶ resistivity,⁴⁷ and optics⁴⁸ suggest that electron correlations are essential to the underlying physical picture in CrO_2 . Schwarz⁴⁹ first predicted the half-metallic band structure with a spin moment of $2 \mu_B$ per formula unit for CrO_2 . Later on Lewis⁴¹ used the plane-wave potential method and investigated the energy bands and the transport properties, characterizing CrO_2 as a "bad metal," terminology applied to high temperature superconductors, or to the other transition metal oxides, even ferromagnets such as SrRuO_3 . A decade later the LSDA+U calculation⁴² explained the conductivity in the presence of large on-site Coulomb interactions, and concluded that CrO_2 is a negative charge transfer gap material which leads to self-doping. Contrary to the on-site strong correlation description, transport and optical properties obtained within the FLAPW method (LSDA and GGA),⁵⁰ suggest that the electron-magnon scattering is responsible for the renormalization of the one-electron bands. In addition, more recent model calculations proposed even orbital correlations.⁵¹

1. Chemical bonding and the Cr- t_{2g} Wannier orbitals

Chemical bonding in rutile-type compounds including CrO_2 was analyzed by Sorantin and Schwarz.⁵² Let us summarize their results: one can see that around the Fermi level, the bands are primarily chromium 3d states of t_{2g} manifold, with e_g bands situated higher in energy due to the crystal-field splitting. In the spin polarized case, the exchange splitting shifts the minority spin bands above the Fermi level, as seen in Fig. 7. For the majority t_{2g} bands the Fermi level is lying in a pseudo-gap. Oxygen p-chromium d, hybridization creates both bonding and antibonding hybrid orbitals, with the bonding orbital appearing in the occupied part and the antibonding hybrid orbital remaining in the Cr t_{2g} manifold. Half of the d_{yz} and d_{zx} components of t_{2g} are pushed upward, by antibonding, that explains the dominance of d_{xy} character in the spin density. The non-magnetic density of states shows a sharp peak at the Fermi level, which signals the magnetic instability according to the usual Stoner argument.

By the procedure of NMTOs we can easily gain a more complete picture about the chemical bonding. In Fig. 8 the non-spin-polarized band structure of CrO_2 is calculated with the full basis set (thick green line). Cr e_g , Cr t_{2g} , and O p states are lying between 1.5-5 eV, 1-1.5 eV, and -7.5-1.5 eV, respectively. There is an excellent agreement with the previous calculations.^{42,49,50,52} The thin red bands have been calculated with the downfolded basis set which includes only Cr-d orbitals. The energy mesh used in the downfolded calculation is given to the right of the band structure. NMTO Cr- t_{2g} Wannier orbitals at Cr1 (0, 0, 0) and Cr2 ($\frac{1}{2}, \frac{1}{2}, \frac{1}{2}$) are shown in Fig. 9. All t_{2g} orbitals form antibonding pd coupling with O-2p states. These antibonding NMTO Wannier orbitals capture the essentials to describe the half-

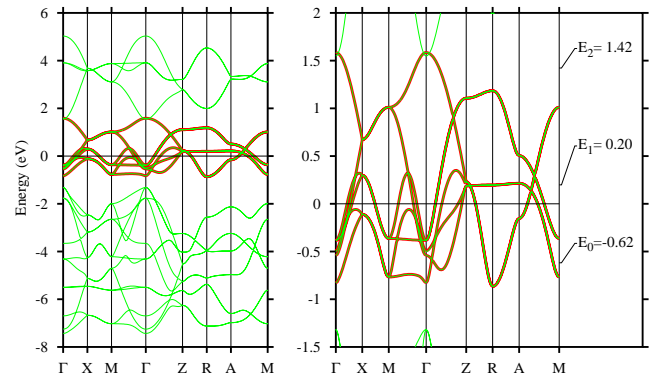


FIG. 8: (Color online) The band structure of non-spin-polarized CrO_2 calculated with the full basis is given in thick (green) line. The thin (red) band have been calculated with a Cr- t_{2g} NMTO basis set. Energy mesh used for downfolded calculation is given in the right of the band structure with a unit of eV. About symmetry points and E_F , see Fig. 7.

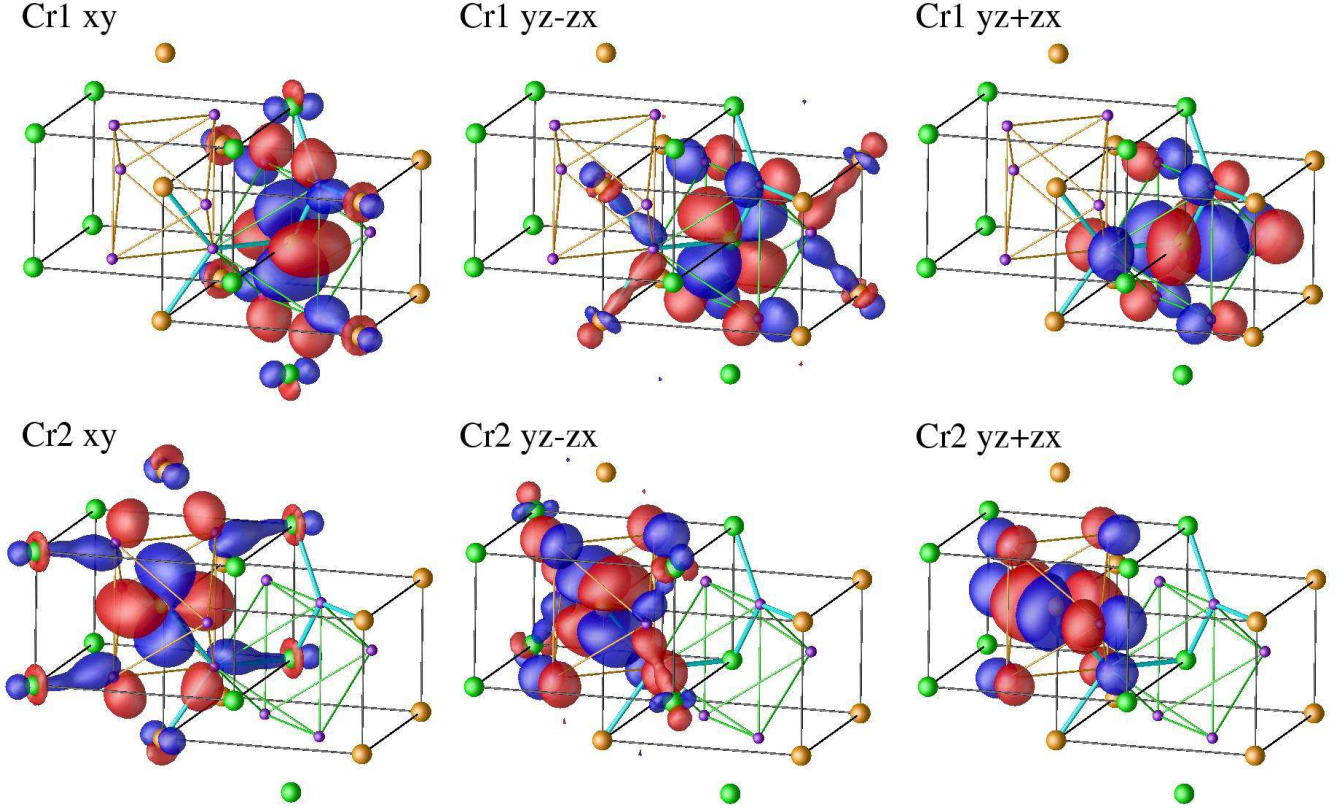


FIG. 9: (Color) NM TO Cr-t_{2g} Wannier orbitals of CrO_2 . Cr1 is orange, Cr2 is green, and O is purple. The local coordinate systems are used for each atom. Red (blue) indicates a positive (negative) sign. Upper panel: Cr1 t_{2g} orbitals. Lower panel: Cr2 t_{2g} orbitals. d_{xy} (left). This orbital is singly degenerated. d_{yz-zx} (middle) and d_{yz+zx} (right). These two orbitals are nearly degenerated.

metallicity of CrO_2 .

Note that the local coordinate system is used.⁵³ For instance, the z axis at Cr1 site points along the $[110]$, while the z axis at Cr2 sites points towards the $[1\bar{1}0]$ direction. In the following we describe the essential features of the Cr- d and O- $2p$ orbital couplings in the t_{2g} orbitals on Cr1 site:

(i) Cr_3O cluster. The oxygen atoms yield a Cr_3O cluster with three surrounding Cr atoms. The Cr1 atom has six Cr_3O clusters with two different types; for instance, one Cr_3O cluster is formed by Cr1 at $(0,0,0)$ and $(0,0,1)$, Cr2 at $(\frac{1}{2}, \frac{1}{2}, \frac{1}{2})$, and O at $(u, \frac{1}{2}, \frac{1}{2})$ in the (110) plane. Another type of Cr_3O cluster is formed by Cr1 at $(0,0,0)$, Cr2 at $(\frac{1}{2}, \frac{1}{2}, \frac{1}{2})$, and O at $(u, u, 0)$ in the (110) plane. The O is sitting in the center of a triangle formed by the three coplanar Cr nearest atoms. The Cr_3O cluster is indicated by thick cyan lines in Fig. 9. In the Cr_3O unit, one can see one antibonding pd coupling between Cr-t_{2g} and O- p states and two bonding pd couplings between Cr-e_g and O- p states. On one hand, the Cr-e_g and Cr-t_{2g} orbitals lying within the Cr_3O plane couple to the in-plane O- p orbital. On the other hand, the out-of-plane O- p orbital component, perpendicular to the Cr_3O plane, cannot couple to the Cr-e_g state due to orthogonality.

(ii) d_{xy} orbitals. The Cr1 atom experiences a bonding coupling between its d_{xy} orbital and the e_g (d_{3z^2-1}) orbital located on the other six nearest Cr atoms on the (110) plane via Cr_3O cluster. The bonding is realized via the tails of O- $2p$ (p_x - and p_y -like) orbitals. e_g tails belonging to the first NN Cr1 $(0,0,1)$ and second NN Cr2 $(\frac{1}{2}, \frac{1}{2}, \frac{1}{2})$, $(\frac{1}{2}, \frac{1}{2}, \frac{1}{2})$ atoms are visible in the (110) plane, where the d_{xy} orbital is situated. Further, the d_{3z^2-1} state belonging to the Cr1 $(0,0,1)$ atom forms a pd -type bonding with both O p_x orbital located at $(u, \frac{1}{2}, \frac{1}{2})$ and $(u, \frac{1}{2}, \frac{1}{2})$ and with O p_y situated at $(\frac{1}{2}, u, u)$ and $(\frac{1}{2}, \frac{1}{2}, \frac{1}{2})$. The d_{xy} orbital, on the contrary, forms an antibonding coupling with these O p_x and O p_y states. Cr2 atom situated at $(\frac{1}{2}, \frac{1}{2}, \frac{1}{2})$ involves its d_{3z^2-1} orbital into a pd bonding with O p_x orbital situated at $(u, \frac{1}{2}, \frac{1}{2})$ and $(u, \frac{1}{2}, \frac{1}{2})$.

(iii) d_{yz-zx} orbitals. The O atoms situated at $(u, u, 0)$ and $(u, u, 0)$ intermediate a pd bonding, via their p_x p_y orbital, between the d_{yz-zx} orbital at Cr1 $(0,0,0)$ and the e_g orbitals at Cr2 $(\frac{1}{2}, \frac{1}{2}, \frac{1}{2})$ and $(\frac{1}{2}, \frac{1}{2}, \frac{1}{2})$ atoms. This bonding orbital is situated in the (110) plane similarly to the d_{yz-zx} orbital. However, its bonding strength seems to be weaker than the ones of the d_{xy} orbitals, due to a larger distance between O and Cr2 atoms. The O p_z orbitals belonging to the atoms situated

at $(\frac{1}{2}, u, u, \frac{1}{2}, \frac{1}{2})$ and $(u, \frac{1}{2}, \frac{1}{2}, u, \frac{1}{2})$, form a pd coupling with d_{yz-zx} orbital. Therefore the O p_z orbital perpendicular to the plane of the Cr_3O cluster does not overlap with the e_g tails of Cr1 (0,0,1) atoms sitting along the [001] direction.

(iv) d_{yz+zx} orbitals. The e_g tails can not contribute at all to the d_{yz+zx} orbital. Because O p_z orbitals at $(\frac{1}{2}, u, u, \frac{1}{2}, \frac{1}{2})$, $(u, \frac{1}{2}, \frac{1}{2}, u, \frac{1}{2})$ and O p_{x+y} orbitals at $(u, u, 0)$, $(u, u, 0)$ are situated perpendicular to Cr_3O clusters, the coupling between O p (p_z and p_{x+y}) states and e_g states at surrounding Cr atoms is not allowed due to the orthogonality.

We discussed in the above points (i)-(iv), the direct or mediated interactions between Cr-d and O-p or between the Cr t_{2g} and e_g states. As it is already known,^{42,49,50,52} there is a significant difference between the t_{2g} and e_g orbitals, however the above analysis in the framework of NMT O technique shows that their interplay constitutes an important ingredient not only for the crystal-field splitting of t_{2g} states, but also for the general bonding in the rutile structure. The t_{2g} orbitals form the basis set in which the effective hopping Hamiltonian matrix elements are evaluated. These results are presented below.

2. Effective hopping matrix elements in the Cr t_{2g} Wannier orbitals

The hopping integrals with t_{2g} Wannier representation up to the second NN are as follows.

NMT O basis set:

$$|t_{2g}\rangle = f|xyi\rangle; |yz-zxi\rangle; |yz+zxig\rangle; \quad (7)$$

The on-site term :

$$t_{m\ 0\ m}^{000} = \begin{pmatrix} 0 & 104 & 0 & 0 \\ 0 & 323 & 0 & 0 \\ 0 & 0 & 355 & 0 \end{pmatrix} \text{ eV} : \quad (8)$$

The first nearest neighbor:

$$t_{m\ 0\ m}^{001}(\text{Cr1}! \text{Cr1}) = \begin{pmatrix} 0 & 119 & 0 & 0 \\ 0 & 0 & 177 & 0 \\ 0 & 0 & 0 & 196 \end{pmatrix} \text{ eV} : \quad (9)$$

The second nearest neighbor:

$$t_{m\ 0\ m}^{\frac{1}{2}\frac{1}{2}\frac{1}{2}}(\text{Cr1}! \text{Cr2}) = \begin{pmatrix} 0 & 4 & 0 & 0 \\ 32 & 0 & 0 & 0 \\ 0 & 204 & 142 & 0 \end{pmatrix} \text{ eV} ; \quad (10)$$

where the unit is meV and a local coordinate system for each atom Cr1 and Cr2 in the unit cell is used as seen in Fig. 6. The on-site term $t_{m\ 0\ m}^{000}$ and the first NN hoppings are diagonal in a $(d_{xy}; d_{yz-zx}; d_{yz+zx})$ representation. The splitting between these orbitals is due partly to the orthorhombic distortion of CrO_6 octahedra and partly to the bonding with the e_g states of nearest Cr atoms in rutile structure. As a consequence mainly two

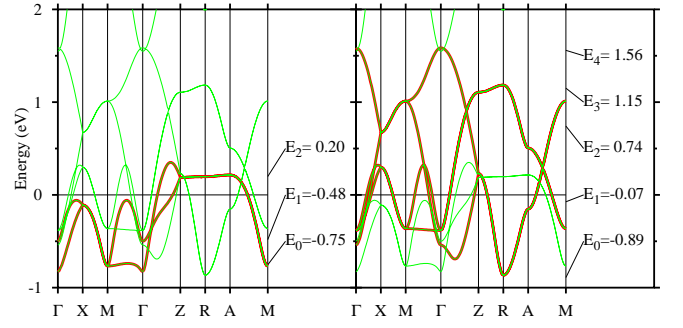


FIG. 10: (Color online) NMT O downfolded d_{xy} (left) and d_{yz-zx} (right) bands for CrO_2 . Energy mesh used for each calculation is given in the right of the band structure with a unit of eV. For symmetry points and E_F , see Fig. 7.

crystal-field levels are formed, a single d_{xy} and two nearly degenerate d_{yz-zx} orbitals situated with 235 meV at higher energies, that can be derived from the difference between on-site levels of d_{xy} and d_{yz-zx} orbitals in Eq. (8). A possible ingredient in determining the position of the nearly degenerate d_{yz-zx} orbitals with respect to the single d_{xy} orbital is the bond length between Cr and O atoms. In the calculations presented in this paper a longer bond length along z direction ($d_z = 1.91$ Å) is used in comparison with the bond formed in the xy plane having a value of ($d_k = 1.89$ Å). In another experiment, however, the opposite situation is reported, $d_z = 1.89$ Å is smaller than $d_k = 1.91$ Å.⁵⁴ In both cases, however, the band structure and density of states are almost identical. Moreover other oxides (TiO_2 , VO_2 etc.) with rutile structure have a similar band structure and density of states for t_{2g} states. This fact suggests that the bonding with e_g state is essential for the crystal-field splitting of t_{2g} states. Similar mechanism for the crystal-field splitting of t_{2g} state is realized in V_2O_3 (Ref. 55) and $NaCoO_2$.⁵⁶

There are two first NN between Cr1 (Cr2) and eight second NN hoppings between Cr1 and Cr2. Only one hopping integral at each NN is shown here. The hopping integrals are strongly affected by Wannier function's tails which are mainly due to downfolded O 2p and Cr e_g orbitals. d_{xy} orbital has a small second nearest hopping integrals $t_{xy\ xy}^{\frac{1}{2}\frac{1}{2}\frac{1}{2}} = 4$ meV although O p tails are present. This means that d_{xy} orbital does not have the second NN hopping path, indicating a very narrow d_{xy} band. On contrary, large hopping integrals of the second NN are shown in d_{yz-zx} block. d_{yz+zx} orbitals can hop to d_{yz+zx} of all direction ($t_{yz+zx\ yz+zx}^{2nd\ NN} = 142$ meV), but d_{yz-zx} can not to d_{yz-zx} ($t_{yz-zx\ yz-zx}^{2nd\ NN} = 0$ meV exactly, as a consequence of orthogonality.) The hopping between d_{yz-zx} and d_{yz+zx} ($t_{yz-zx\ yz+zx} = 204$ meV) is allowed for a particular direction, that is, the second NN hopping from Cr1 d_{yz+zx} to Cr2 d_{yz-zx} sitting in (110) plane or from Cr1 d_{yz-zx} to Cr2 d_{yz+zx} sitting in (110) plane. The large values of second NN hopping in d_{yz-zx} block are caused by O p

tails which are not orthogonal to each other, and induce both the itinerant property and the wide band of $d_{yz\ zx}$ states. $d_{yz\ zx}$ orbitals have the second NN hopping path via O p tails. Moreover the large off-diagonal hopping integral of second NN and the small crystal-field splitting between $d_{yz\ zx}$ indicate that $d_{yz\ zx}$ states should be treated together. The Cr1 $d_{yz\ zx}$ orbital is weakly coupled with Cr2 d_{xy} ($t_{xy;xy} = 32$ meV) along particular directions, within the (110) plane. Hoppings towards the third NN are small; for instance, the largest values are 45 meV (third) and 30 meV (fourth and fifth), and the others are almost zero. Further away NN hoppings are much smaller.

Exceptions are, however, the e_g tails of Wannier function which gives a few large hopping integrals, for instance, $t_{xy;xy}^{002(\text{Cr1! Cr1})} = 82$ meV, $t_{xy;xy}^{110(\text{Cr1! Cr1})} = 95$ meV, and $t_{yz\ zx;yz\ zx}^{11\frac{1}{2}(\text{Cr1! Cr1})} = 50$ meV. These large hoppings can be seen in Fig. 9.

3. Effective hopping matrix elements in the independent d_{xy} and $d_{yz\ zx}$ Wannier orbitals

As seen in Eqs. (8)-(10), the coupling between d_{xy} and $d_{yz\ zx}$ seems to be weak. The NMTO method may be able to pick up such bands independently. The d_{xy} and $d_{yz\ zx}$ bands are shown in Fig. 10. The Wannier orbitals are more extended due to additional downfolding. This affects the hopping integrals as well. The hopping integrals with d_{xy} and $d_{yz\ zx}$ Wannier representation up to the second NN are as follows.

NMTO basis set:

$$\tau = f_{jxy}; f_{jyz\ zx}; i; jz + x; i; jz + x; i; jz + x : \quad (11)$$

The on-site term :

$$t_{m\ 0; m\ 0}^{000} = \begin{pmatrix} 0 & & 1 \\ & 24 & \\ 312 & 0 & A \\ 0 & 373 & \end{pmatrix} : \quad (12)$$

The first nearest neighbor:

$$t_{m\ 0; m\ 0}^{001(\text{Cr1! Cr1})} = \begin{pmatrix} 0 & & 1 \\ & 99 & \\ 187 & 0 & A \\ 0 & 197 & \end{pmatrix} : \quad (13)$$

The second nearest neighbor:

$$t_{m\ 0; m\ 0}^{\frac{1}{2}\frac{1}{2}\frac{1}{2}(\text{Cr1! Cr2})} = \begin{pmatrix} 0 & & 1 \\ & 26 & \\ 0 & 0 & A \\ 202 & 135 & \end{pmatrix} ; \quad (14)$$

where the same definitions of Eqs. (7)-(10) are used. Since the Wannier orbitals are more extended the hoppings are modified slightly, but not changed significantly. A few large hoppings of far NN are also reduced; $t_{xy;xy}^{002(\text{Cr1! Cr1})} = 21$ meV, $t_{xy;xy}^{110(\text{Cr1! Cr1})} = 16$ meV, and $t_{yz\ zx;yz\ zx}^{11\frac{1}{2}(\text{Cr1! Cr1})} = 39$ meV. In addition, there is no

matrix elements in LDA Hamiltonian between d_{xy} and $d_{yz\ zx}$ block, that is there is no LDA interaction between them, by virtue of our construction of NMTO Wannier functions.

The possibly minimal set of Wannier function may provide new insights. At the first glance one can separate the narrow d_{xy} orbitals from the extended $d_{yz\ zx}$ states. The former would be treated as corelike (classical) spin $S = 1=2$, meanwhile in the later dispersive $d_{yz\ zx}$ bands the Coulomb repulsion would be treated in a usual quantum many-body way. Such a Kondo-lattice type model, for CrO_2 would be described by the following Hamiltonian:

$$H = \sum_{i,j;m\ 0} t_{ij}^{m\ m\ 0} C_{im}^y C_{jm\ 0} + \sum_{i;m} J S_{i;d_{xy}}^z (C_{im}^y C_{im}^y - C_{im}^y C_{im}^y) + \frac{1}{2} (S_{i;d_{xy}}^+ C_{im}^y C_{im}^y + S_{i;d_{xy}}^- C_{im}^y C_{im}^y) : \quad (15)$$

The first term denotes the hopping of the conduction electrons between the NN sites $i; j$ with a hopping matrix element $t_{ij}^{m\ m\ 0}$ between the $d_{yz\ zx}$ orbitals, described by the $m; m\ 0$ indices. The $d_{yz\ zx}$ electrons and the localized d_{xy} spins interaction is given by the second term as an exchange coupling ($J < 0$ for antiferromagnetic and $J > 0$ for ferromagnetic coupling). The ferromagnetic coupling between the core spins and conduction electrons, favors ferromagnetic ordering, because the hopping amplitudes of the conduction electrons reach the maximum possible values if the core spins are aligned. Many of the Mn-type colossal magnetoresistance materials (CMR) can be described by such a model. Recently a realistic LDA+DMFT calculation for such a model is carried out.⁵⁷ The d shell of the Mn^{3+} in the undoped antiferromagnetic insulator contains three electrons in the t_{2g} orbitals forming a core spin of magnitude $S = 3=2$, which due to strong Hund's rule coupling couples ferromagnetically to one additional electron in one of the e_g orbitals. For a certain doping CMR materials are ferromagnetic metals because of additional holes in the e_g conduction bands.

In contrast to the manganites, in CrO_2 , the d_{xy} spin has a smaller value $S = 1=2$, and the splitting of the localized d_{xy} orbital with respect to the itinerant $d_{yz\ zx}$ one is smaller [~ 370 meV, see. Eq. (12)].

It was shown recently⁵⁸ that for a proper definition of the many-body green function in CrO_2 , the complete t_{2g} manifold is required. Moreover a better description of polarization can be obtained considering the competition between quasiparticle description around the Fermi level, and a local moment behavior at higher energies, above the Fermi level.⁵⁸

According to our results, NMTO can give a minimal model with a possibly minimal set of distinct Wannier d_{xy} and $d_{yz\ zx}$ functions. This result does not exclude

the possibility of integrating out the degrees of freedom connected to the narrow/extended d_{xy}/d_{yz} orbitals. Physically this would correspond to the dualistic character of the electronic structure of CrO_2 around the Fermi level.⁵⁹

III. EFFECTIVE COULOMB REPULSION

The other essential component for a model Hamiltonian describing correlations, is the average Coulomb interaction parameter U . This term acts on the diagonal part of the effective Hamiltonian and corresponds to the screened electron-electron repulsion. Aryasetiawan et al. pointed out recently⁶⁰ that a rigorous way to define this quantity can be formulated in terms of path integrals by performing a partial trace, over the degrees of freedom, that one wants to eliminate. However, in practice for realistic materials, the elimination of degrees of freedom is a very difficult procedure.

In order to evaluate the average Coulomb interaction on the d atoms and the corresponding exchange interactions we start with the constrained LDA method.^{61,62,63,64,65,66} In this approach the Hubbard U is calculated from the total energy variation with respect to the occupation number of the localized orbitals. In such a scheme the metallic screening is rather inefficient for 3d transition metals.⁶⁶ The perfect metallic screening will lead to a smaller value of U . Unfortunately, there are no reliable schemes to calculate U in metals,⁶⁷ therefore in our previous works^{23,24,25,26} we choose some intermediate values of U from 2 to 4.8 eV and $J = 0.9$ eV.

In the case of NiMnSb the constrained LDA calculation indicates that the average Coulomb interaction between the Mn 3d electrons is about $U = 4.8$ eV with an exchange interaction energy about $J = 0.9$ eV as seen in Table II. A reduced value of U can be obtained if one considers that the Mn e_g orbitals participate in the screening of Mn t_{2g} ,^{68,69} reducing the average Coulomb interaction on the Mn atoms to a value of $U = 4.2$ eV. However, our DMFT results²³ showed that the many-body effects are equally essential for t_{2g} and e_g orbitals, therefore a model with only Mn t_{2g} , even if it may capture the main physical results, would suffer of incompleteness. Note that physical results for NiMnSb are not very sensitive to the value of U , as it was demonstrated.²³

TABLE II: The constrained LDA values of the average Coulomb and exchange interactions. The second row corresponds to the results when the e_g orbitals screen the t_{2g} ones. This type of screening would be more appropriate for the CrO_2 case.

	NiMnSb		CrO ₂	
	U (eV)	J (eV)	U (eV)	J (eV)
t_{2g} and e_g	4.80	0.93	3.50	0.90
t_{2g}	4.25	0.93	3.00	0.87

Concerning the local Coulomb interaction U , in CrO_2 , we saw from the analysis of the Cr-3d manifold that the higher energy e_g bands make no noticeable contribution to the Fermi level, however they could participate in the screening of the t_{2g} orbitals,^{68,69} giving the following values for $U = 3$ eV and $J = 0.87$ eV.

IV. SUMMARY

Spintronics requires the search for new materials such as half-metallic ferromagnets, whose properties are commanded by their electronic structure and electron-electron correlations. To understand the collective effects a clear picture of the interplay between the microscopic interactions is necessary. Model Hamiltonians allow a controlled reduction of the *ab initio* information into a few dominant material specific hopping and interaction parameters. In this paper we have applied the downfolding procedure within the N th order multi-orbital (NMO) method to obtain model Hamiltonian parameters for two ferromagnetic half-metallic NiMnSb and CrO_2 .

For NiMnSb , the present Wannier orbital results confirm the previous conclusions of Ref. [4] based on the gamma point analysis. However based on the whole Brillouin zone analysis we found that d-d hybridization between the transition metal atoms is essential for the gap formation as the p-d hybridization previously discussed.⁴ Due to the significant Mn exchange splitting, a different hybridization takes place in the spin-up and spin-down channels, which determines the appearance of the gap only for spin-down electrons meanwhile for spin-up states a metallic character is evidenced.

A downfolding calculations which would include the Sb-p and Ni-d orbitals, would increase considerably the computational demand. However, the physical picture would not be very much changed, because an antibonding Mn d Wannier orbital including Sb p and Ni d character as a tail should play an important role for half-metallic nature around Fermi level. Therefore, the effective Hamiltonian described by Eqs. (4)-(6), represents a good starting point to investigate many-body effects.

Accordingly many-body correlation effects would be of primary importance for the Mn orbitals the Ni one could be neglected. In our previous many-body results^{23,24} we made use of the above conclusions, so correlation effects were considered only for Mn-d orbitals. The LDA+DMFT results showed the existence of non-quasiparticle states (NQP) state^{27,28} in the minority spin channel. These states are associated with finite temperature spin fluctuation processes which play an important role in depolarization. In the majority spin channel, FeMnSb (Ref. 24) has a larger DOS at the Fermi level in comparison with NiMnSb .²³ This contributes to a stronger finite temperature depolarization in FeMnSb , which increase with the on-site Coulomb interaction.

For CrO_2 the bands around the Fermi level are primarily chromium 3d states of t_{2g} manifold, with e_g bands

situated higher in energy by the crystal-field splitting. The t_{2g} orbitals are further splitted into a single d_{xy} and nearly degenerate d_{yz-zx} bands due to the orthorhombic distortion of CrO_6 octahedra. We discussed the direct and the mediated Cr- d , O- p , or Cr t_{2g} - e_g interactions. Despite the differences between Cr t_{2g} - e_g orbitals their interaction play an important role not only in characterizing the crystal-field splitting, but also in the general picture of bonding in the rutile structure.

The basis set of the Wannier orbitals for CrO_2 is formed in t_{2g} manifold. In the framework of the NMO technique two distinct downfolding procedures are possible.

In the first approach a full t_{2g} construction is possible, i.e., a single d_{xy} and a nearly degenerate d_{yz-zx} orbitals represents the basis set. We believe that such a basis set can be used in connection with the multi-orbital Hubbard Hamiltonian described in Eq. (1).

A second approach is made possible due to a weak d_{xy} and d_{yz-zx} coupling. In this case the lowest d_{xy} and the higher d_{yz-zx} bands can be derived separately as shown in Fig. 10. For such a situation, downfolded NMO

Hamiltonian with a set of those Wannier orbitals $fd_{xy}g$ and $fd_{yz-zx}g$, $d_{yz-zx}g$, is block diagonal, that is, there is no hopping between the lowest d_{xy} and the higher d_{yz-zx} orbitals. This fact gives a strong impression for a Kondo-lattice type model Hamiltonian described by Eq. (15). In a future work we report on the qualitative/quantitative differences of such models applied to CrO_2 .

Similarly to our previous DMFT results on semiconductors^{23,24} and zinc-blende structures,^{25,26} further work will include the many body effects in CrO_2 and the analysis of nature of the NQP states in these classes of half-metallic ferromagnets.

Acknowledgments

We are grateful for enlightening discussions with R. A. de Groot, O. Jepsen, O. Gunnarsson, K. Held, and E. Arrigoni. L.C. acknowledges financial support offered by the Austrian Science Foundation FWF Project No. P18505-N16.

Electronic address: A.Yamasaki@fkf.mpg.de

- ¹ V. Yu. Irkhin and M. I. Katsnelson, *Usp. Fiz. Nauk* 164, 705 (1994) [*Phys. Usp.* 37, 659 (1994)].
- ² S. A. Wolf, D. D. Awschalom, R. A. Buhrman, J. M. Daughton, S. von Molnar, M. L. Roukes, A. Y. Chtchelkanova, and D. M. Treger, *Science* 294, 1488 (2001).
- ³ I. Zutic, J. Fabian, and S. Das Sarma, *Rev. Mod. Phys.* 76, 323 (2004).
- ⁴ R. A. de Groot, F. M. Mueller, P. G. van Engen, and K. H. J. Buschow, *Phys. Rev. Lett.* 50, 2024 (1983).
- ⁵ R. J. Soulen, Jr., M. Byers, M. S. Osofsky, B. Nadgorny, T. Ambrose, S. F. Cheng, P. R. Broussard, C. T. Tanaka, J. Nowak, J. S. Moodera, A. Barry, and J. M. D. Coey, *Science* 282, 85 (1998); R. J. Soulen, Jr., M. S. Osofsky, B. Nadgorny, T. Ambrose, P. Broussard, S. F. Cheng, J. M. Byers, C. T. Tanaka, J. Nowak, J. S. Moodera, G. Laprade, A. Barry, and M. D. Coey, *J. Appl. Phys.* 85, 4589 (1999).
- ⁶ S. K. Choe, Y. Miyoshi, Y. Bugoslavsky, W. R. Branford, C. G. Rigorescu, S. A. Mamea, O. Monneanu, and L. F. Cohen, *Phys. Rev. B* 69, 214425 (2004).
- ⁷ W. Zhu, B. Sinkovic, E. Vescovo, C. Tanaka, and J. S. Moodera, *Phys. Rev. B* 64, 060403(R) (2001).
- ⁸ M. Siot, P. Turban, S. Andrieu, A. Tagliaferri, C. De Nadai, N. B. Brookes, F. Bertran, and F. Fortuna, *J. Magn. Magn. Mater.* 303, 54 (2006).
- ⁹ G. A. de Wijs and R. A. de Groot, *Phys. Rev. B* 64, 020402(R) (2001).
- ¹⁰ Y. Ji, G. J. Strijkers, F. Y. Yang, C. L. Chien, J. M. Byers, A. Anguelbuch, G. Xiao, and A. Gupta, *Phys. Rev. Lett.* 86, 5585 (2001).
- ¹¹ J. S. Parker, S. M. Watts, P. G. Ivanov, and P. Xiong, *Phys. Rev. Lett.* 88, 196601 (2002).
- ¹² Y. S. Dedkov, M. Fonine, C. Konig, U. Rudiger, G. Guntherodt, S. Senz, and D. Hesse, *Appl. Phys. Lett.* 80, 4181 (2002).
- ¹³ J. M. D. Coey, J. Versluijs, and M. Venkatesen, *J. Phys. D* 35, 2457 (2002).
- ¹⁴ R. S. Keizer, S. T. B. Goennenwein, T. M. Klapwijk, G. Miao, G. Xiao, and A. Gupta, *Nature (London)* 439, 825 (2006).
- ¹⁵ A. I. Lichtenstein and M. I. Katsnelson, *Phys. Rev. B* 57, 6884 (1998).
- ¹⁶ W. Metzner and D. Vollhardt, *Phys. Rev. Lett.* 62, 324 (1989).
- ¹⁷ A. Georges, G. Kotliar, W. Krauth, and M. Rozenberg, *Rev. Mod. Phys.* 68, 13 (1996).
- ¹⁸ V. I. Anisimov, A. I. Poteryaev, M. A. Korotin, A. O. Anokhin, and G. Kotliar, *J. Phys.: Condens. Matter* 9, 7359 (1997).
- ¹⁹ M. I. Katsnelson and A. I. Lichtenstein, *J. Phys.: Condens. Matter* 11, 1037 (1999).
- ²⁰ K. Held, I. A. Nekrasov, G. Keller, V. Eyert, N. Blümer, A. K. M. Chahan, R. T. Scalettar, Th. Pruschke, V. I. Anisimov, and D. Vollhardt, *Phys. Rev. Lett.* 86, 65 (2003) [http://psik.diac.uk/newletters/New_s56/Highlight_56.pdf].
- ²¹ L. Chioncel, L. Vitos, I. A. Abrikosov, J. Kollar, M. I. Katsnelson, and A. I. Lichtenstein, *Phys. Rev. B* 67, 235106 (2003).
- ²² G. Kotliar and D. Vollhardt, *Phys. Today* 57, 53 (2004); G. Kotliar, S. Y. Savrasov, K. Haule, V. S. Oudovenko, O. Parcollet, and C. A. Marianetti, to be published in *Rev. Mod. Phys.* 78 (2006), cond-mat/0511085.
- ²³ L. Chioncel, M. I. Katsnelson, R. A. de Groot, and A. I. Lichtenstein, *Phys. Rev. B* 68, 144425 (2003).
- ²⁴ L. Chioncel, E. Arrigoni, M. I. Katsnelson, and A. I. Lichtenstein, *Phys. Rev. Lett.* 96, 137203 (2006).
- ²⁵ L. Chioncel, M. I. Katsnelson, G. A. de Wijs, R. A. de Groot, and A. I. Lichtenstein, *Phys. Rev. B* 71, 085111 (2005).

- ²⁶ L.Chioncel, Ph.M avropoulos, M .Lezaic, S.B lügel, E .A r-
righoni, M .I.K atsnelson, and A .I. Lichtenstein, *Phys. Rev.*
Lett. 96, 197203 (2006).
- ²⁷ D .M .Edwards and J.A .Hertz, *J. Phys. F* 3, 2191 (1973).
- ²⁸ V .Yu. Irkhin and M .I. Katsnelson, *Fizika Tverdogo Tela*
25, 3383 (1983) [*Sov. Phys. - Solid State* 25, 1947 (1983)];
J. Phys. : Condens. Matter 2, 7151 (1990).
- ²⁹ B .Sanyal, L.B ergqvist, and O .E riksson, *Phys. Rev. B* 68,
054417 (2003).
- ³⁰ O .K .Andersen and T .Saha-D asgupta, *Phys. Rev. B* 62,
R16219 (2000); O .K .Andersen, O .Jepsen, and G .K rier,
in *Methods of Electronic Structure Calculations*, edited by
V .K um ar, O .K .Andersen, and A .M ookerjē (W orld Sci-
enti c, Singapore, 1994), pp. 63{124; O .K .Andersen, T .
Saha-D asgupta, R .W .Tank, C .A rcangeli, O .Jepsen, and
G .K rier, in *Electronic Structure and Physical Properties*
of Solids. The Uses of the LM TO M ethod, edited by H .
D reyse, Springer Lecture Notes in Physics (Springer, New
York, 2000), pp. 3{84; O .K .Andersen, T .Saha-D asgupta,
S .Ezhov, L .T setseris, O .Jepsen, R .W .Tank, C .A r-
cangeli, and G .K rier, *Psik Newsletter* # 45, 86 (2001)
[http://psik.diac.uk/newletters/New_s45/Highlight_45.pdf].
- ³¹ E .Zurek, O .Jepsen, and O .K .Andersen, *Chem Phys Chem*
6, 1934 (2005).
- ³² O .K .Andersen, *Phys. Rev. B* 12, 3060 (1975).
- ³³ O .K .Andersen and O .Jepsen, *Phys. Rev. Lett.* 53, 2571
(1984).
- ³⁴ The Stuttgart TB-LM TO-ASA code, version 4.7. See:
<http://www.fkf.mpg.de/andersen/>.
- ³⁵ E .Pavarini, A .Yam asaki, J. Nuss, and O .K .Andersen,
New J. Phys. 7, 188 (2005).
- ³⁶ S .O gut and K .M .Rabe, *Phys. Rev. B* 51, 10443 (1995).
- ³⁷ I .Galanakis, P .H .D ederichs, and N .Papanikolaou, *Phys.*
Rev. B 66, 134428 (2002).
- ³⁸ B .R .K .Nanda and I .D asgupta, *J. Phys.: Condens. Matter* 15,
7307 (2003).
- ³⁹ E .K ulatov and I .I. M azin, *J. Phys.: Condens. Matter* 2,
343 (1990).
- ⁴⁰ B .J. Thamer, R .M .D ouglass, and E .Staritzky, *J. Am .*
Chem .Soc. 79, 547 (1957).
- ⁴¹ S .P. Lewis, P .B .A llen and T .Sasaki, *Phys. Rev. B* 55,
10253 (1997).
- ⁴² M .A .K orotin, V .I. Anisim ov, D .I. Khom skii, and G .A .
Sawatzky, *Phys. Rev. Lett.* 80, 4305 (1998).
- ⁴³ P .Schlottmann, *Phys. Rev. B* 67, 174419 (2003).
- ⁴⁴ B .I. Chamberland, *CRC Crit. Rev. Solid State Mater. Sci.*
7, 1 (1977).
- ⁴⁵ T .T sujōka, T .M izokawa, J .O kam oto, A .Fujim ori, M .
Nohara, H .Takagi, K .Yam aura, and M .Takano, *Phys.*
Rev. B 56, R15509 (1997).
- ⁴⁶ C .B .Stagarescu, X .Su, D .E .Eastm an, K .N .A ltm ann, F .
J.H impsel, and A .G upta, *Phys. Rev. B* 61, R9233 (2000).
- ⁴⁷ K .Suzuki and P .M .Tedrow, *Phys. Rev. B* 58, 11597
(1998).
- ⁴⁸ E .J. Singley, C .P .W eber, D .N .Basov, A .Barry, and J .
M .D .Coey, *Phys. Rev. B* 60, 4126 (1999).
- ⁴⁹ K .H .Schwarz, *J. Phys. F* 16, L211 (1986).
- ⁵⁰ I .I. M azin, D .J. Singh, and C .A mbrosch-D raxl, *Phys. Rev.*
B 59, 411 (1999).
- ⁵¹ M .S .Laad, L .C raco, and E .M uller-H artm ann, *Phys. Rev.*
B 64, 214421 (2001); L .C raco, M .S .Laad, and E .M uller-
H artm ann, *Phys. Rev. Lett.* 90, 237203 (2003).
- ⁵² P .I. Sorantin and K .Schwarz, *Inorg. Chem .* 31, 567
(1992).
- ⁵³ Note that the local coordinate system in the paper Ref. [52]
is different from the one presented in Ref. [42]. In the
present paper we use the convention presented in the later
Ref. [42].
- ⁵⁴ P .Porta, M .M arezio, J .P .Rem eika, and P .D .D emier,
M ater. Res. Bull. 7, 157 (1972).
- ⁵⁵ T .Saha-D asgupta, O .K .Andersen, J .Nuss, A .P oteryaev,
A .I. Lichtenstein, and A .G eorges (unpublished).
- ⁵⁶ O .K .Andersen, I .I. M azin, O .Jepsen, M .D .Johannes,
and A .Yam asaki (unpublished).
- ⁵⁷ A .Yam asaki, M .Feldbacher, Y .-F .Yang, O .K .Andersen,
and K .H eld, *Phys. Rev. Lett.* 96, 166401 (2006).
- ⁵⁸ M .van Veenendaal and A .J. Fedro, *Phys. Rev. B* 70,
012412 (2004).
- ⁵⁹ D .J. Huang, L .H .T jeng, J .Chen, C .F .Chang, W .P .
W u, S .C .Chung, A .Tanaka, G .Y .Guo, H .-J .Lin, S .G .
Shyu, C .C .W u, and C .T .Chen, *Phys. Rev. B* 67, 214419
(2003).
- ⁶⁰ F .A ryasetiawan, M .Im ada, A .G eorges, G .K otliar, S .
B ierm ann, and A .I. Lichtenstein, *Phys. Rev. B* 70, 195104
(2004).
- ⁶¹ P .H .D ederichs, S .B lügel, R .Zeller, and H .A kai, *Phys.*
Rev. Lett. 53, 2512 (1984).
- ⁶² M .R .Norm an and A .J .Freem an, *Phys. Rev. B* 33, R8896
(1986).
- ⁶³ A .K .M d mahan, R .M .M artin, and S .Satpathy, *Phys.*
Rev. B 38, 6650 (1988).
- ⁶⁴ O .G unnarsson, O .K .Andersen, O .Jepsen, and J .Zaanen,
Phys. Rev. B 39, 1708 (1989).
- ⁶⁵ M .S .Hybertsen, M .Schlüter, and N .E .Christensen,
Phys. Rev. B 39, 9028 (1989).
- ⁶⁶ V .I. Anisim ov and O .G unnarsson, *Phys. Rev. B* 43, 7570
(1991).
- ⁶⁷ For recent progress, see Ref. [60]; I .V .Solov'yev and
M .Im ada, *Phys. Rev. B* 71, 045103 (2005); F .A ryase-
tiawan, K .Karlsson, O .Jepsen, and U .Schonberger,
cond-m at/0603138.
- ⁶⁸ I .Solov'yev, N .Ham ada, and K .Terakura, *Phys. Rev. B*
53, 7158 (1996).
- ⁶⁹ W .E .P ickett, S .C .E rwin, and E .C .E thridge, *Phys. Rev.*
B 58, 1201 (1998).